Hou, Nianjun; Yao, Tongtong; Li, Ping; Yao, Xueli; Gan, Tian; Fan, Lijun; Wang, Jun; Zhi, Xiaojing; Zhao, Yicheng; Li, Yongdan

A-site ordered double perovskite with in situ exsolved core-shell nanoparticles as anode for solid oxide fuel cells

Published in:
ACS Applied Materials and Interfaces

DOI:
10.1021/acsami.8b19928

Published: 20/02/2019

Document Version
Peer-reviewed accepted author manuscript, also known as Final accepted manuscript or Post-print

A-site Ordered Double Perovskite with *in situ* Exsolved Core-Shell Nanoparticles as Anode for Solid Oxide Fuel Cells

Nianjun Hou[a,b], Tongtong Yao[a,b], Ping Li[a,b], Xueli Yao[a,b], Tian Gan[a,b], Lijun Fan[a,b], Jun Wang[a,b], Xiaojing Zhi[a,b], Yicheng Zhao[a,b*], Yongdan Li[a,b,c]

[a]*State Key Laboratory of Chemical Engineering (Tianjin University), Tianjin Key Laboratory of Applied Catalysis Science and Technology, School of Chemical Engineering and Technology, Tianjin University, Tianjin, 300072, China*

[b]*Collaborative Innovation Center of Chemical Science and Engineering (Tianjin) Tianjin, 300072, China.*

[c]*Department of Chemical and Metallurgical Engineering, Aalto University, Kemistintie 1, FI-00076 Aalto, Finland*

*Email: zhaoyicheng@tju.edu.cn

Abstract

A highly active anode material for solid oxide fuel cells resistant to carbon deposition is developed. Co-Fe co-doped $La_{0.5}Ba_{0.5}MnO_{3-\delta}$ with a cubic-hexagonal heterogeneous stucture is synthesized through the pechini method. An A-site ordered double perovskite with $Co_{0.94}Fe_{0.06}$ alloy-oxide core-shell nanoparticles on its surface is formed after reduction. The phase transition and the exsolution of the nanoparticles are investigated with X-ray diffraction, thermogravimetric analysis and high-resolution transmission electron microscope. The exsolved nanoparticles with the layered double perovskite supporter show a high catalytic activity. A single cell with that anode and a 300 μm-thick $La_{0.8}Sr_{0.2}Ga_{0.8}Mg_{0.2}O_{3-\delta}$ electrolyte layer exhibits maximum power densities of 1479 and 503 mW cm^{-2} at 850 ºC with wet hydrogen and wet methane fuels, respectively. Moreover, the single cell fed with wet methane exhibits a stable power output at 850 ºC for 200 h, demonstrating a high resistance to carbon deposition of the anode due to the strong anchor of the exsolved nanoparticles on the perovskite parent. The oxide shell also preserves the metal particles from coking.

Keywords: Anode; Solid oxide fuel cell; *In situ* exsolution; Hydrocarbon; Layered perovskite; Core-shell structure

1. Introduction

Solid oxide fuel cells (SOFCs) are one of the most promising technologies converting chemical energy in fuels into electric power with high efficiency and low emissions. Due to its relatively high operating temperatures (600-1000 ºC), SOFCs offer excellent fuel flexibility, which makes the utilization of the abundance and low cost hydrocarbon fuels possible.[1-3] Methane is a potential fuel for SOFCs due to its abundant reserves and high H/C ratio compared with other hydrocarbons, which results in low CO_2 emissions. However, the strong carbon-hydrogen bonds in CH_4 sluggish its electrochemical oxidation kinetics,[4] and thus the development of anode materials with a sufficient catalytic activity is highly demanded.[5-7] Ni-based cermet anodes face aggregation at high temperature and serious carbon deposition with hydrocarbons as fuels.[8, 9] As promising substitutes, ABO_3 perovskite oxides show a high coking resistance and sulphur tolerance.[10] Nevertheless, most of the perovskite anodes which are stable in a reducing atmosphere, such as chromites, titanates and vanadates, possess either low electrical conductivity or low electrocatalytic activity.[11-14] In 2006, Huang et al.[15] developed a series of double-pervoskite anode materials such as $Sr_2MgMoO_{6-\delta}$ and $Sr_2MnMoO_{6-\delta}$. A single cell with $Sr_2MgMoO_{6-\delta}$ anode and a 300 μm-thick $La_{0.8}Sr_{0.2}Ga_{0.83}Mg_{0.17}O_{2.815}$ electrolyte layer exhibited a maximum power density (P_{max}) of 438 mW cm^{-2} and a quasi-steady performance for 50 power cycles at 800 ºC with dry CH_4 as the fuel.

The coupling of active metallic catalysts and mixed ionic-electronic conducting supporters is a promisng strategy to develop new anode materials with both high catalytic activity and conductivity. However, the conventional infiltration process is time-consuming, and the metallic particles trend to agglomerate at high temperature.[16] Alternatively, catalytic metal atoms can be incorporated into B sites of the host perovskite lattice during the synthesis process in an oxidizing atmosphere and then exsolve as uniform-sized nanoparticles evenly distributed during the following reduction process,

which show high and stable catalytic activity for automotive emissions control.[17, 18] The exsolution in anodes of SOFCs in earlier works were mainly driven by the inherent reducibility of B-site dopant cations, and the exsolved catalysts were limited to precious metals such as Ru,[19, 20] Pt[21] and Pd,[22] and Ni which showed low stability due to agglomeration.[23] In recent years, much effort has been focused on the strategies to facilitate the exsolution, such as A-site deficiency,[24] crystal structure transformation,[25] and electrochemical switching,[26] and the exsolution of cheap and stable transition metals, such as Co, Fe and their alloys, have been widely investigated. A K_2NiF_4-type structured $Pr_{0.8}Sr_{1.2}(Co,Fe)_{0.8}Nb_{0.2}O_{4+\delta}$ material with Co-Fe alloy exsolved on its surface was obtained by annealing perovskite $Pr_{0.4}Sr_{0.6}Co_{0.2}Fe_{0.7}Nb_{0.1}O_{3-\delta}$ in H_2 at 900 °C, and a single cell with that anode achieved P_{max} of 0.6 W cm^{-2} and 0.92 W cm^{-2} at 850 ºC using wet CH_4 and C_3H_8 as fuels, respectively.[27, 28] Very recently, Chen et al.[29] found that the size and iron content of $Co_{1-x}Fe_x$ nanoparticles exsolved from $La_{0.5}Sr_{0.5}Co_{0.45}Fe_{0.45}Nb_{0.1}O_{3-\delta}$ increase with the increase of temperature and reduction time in wet H_2. Lai and Manthiram[30, 31] studied the exsolution and reincorporation of Co-Fe nanoparticles on the surface of $La_{0.3}Sr_{0.7}Cr_{0.3}Fe_{0.6}Co_{0.1}O_{3-\delta}$ during redox cycles at 700-800 ºC. The material shows a high redox reversibility at 700 ºC, bringing about a stable anode performance with H_2 and C_3H_8 as fuels.

A-site ordered double-perovskites $LnBaMn_2O_{5+\delta}$ (Ln means lanthanides such as Pr, Nd and Sm) and their derivatives have been widely investigated as ferromagnetic materials.[32, 33] In the last few years, they have attracted attention as fuel electrodes of SOFCs and solid oxide electrolyzer cells due to their high oxygen ionic diffusion rate and high electronic conductivity.[34-43] A layered structure $[LnO_\delta]$-$[MnO_2]$-[BaO]-$[MnO_2]$-$[LnO_\delta]$ along the *c* axis is formed accompanied with the loss of lattice oxygens during the reduction. The oxygen vacancies formed in the $[LnO_\delta]$ planes facilitate the electrochemical oxidation of fuels and provide two-dimensional channels for the fast conduction of

oxygen ions.[34, 35, 44, 45] A 300 μm-thick $La_{0.9}Sr_{0.1}Ga_{0.8}Mg_{0.2}O_{3-\delta}$ electrolyte-supported single cell with $PrBaMn_2O_{5+\delta}$ (PBM) as the anode obtained a P_{max} of 0.57 W cm^{-2} at 850 °C using H_2 as fuel. In order to improve the catalytic activity of PBM further, late transition metals have been doped in the B sites, and their exsolution is facilitated during the structure transformation. Nanoparticles of metallic Co were exsolved *in situ* from Co-doped PBM and exhibited high catalytic activities towards syngas/ethane oxidation and soot combustion.[39, 46] Fe, Co and Ni were incorporated into the PBM anode, which improved the performance of the SOFCs fed with H_2 and C_3H_8.[36] Nevertheless, the catalytic activities of doped PBM anodes for the electrochemical oxidation of CH_4 are still limited.[34, 40]

$LaMnO_3$ and its derivatives have been widely used as catalysts for complete oxidation of methane.[47-49] Liu et al.[50] investigated $La_{1-x}A_xMnO_3$ (A=Ba, Sr, Ca) as catalysts for methane oxidation, among which $La_{0.8}Ba_{0.2}MnO_3$ showed the highest activity. The conversion of CH_4 oxidation over $La_{0.5}Ba_{0.5}MnO_3$ nanocubes achieved 100% at 600 °C, and maintained at 97% after running at 560 °C for 50 h.[51] Meanwhile, it has been proved that the diffusivity of oxygen in A-site cation ordered perovskite increases with the increase of the radius of the lanthanide element.[44] La^{3+} is a potential candidate for the A-site cation in double-perovskite oxidation catalysts due to its largest size in the lanthanide ions. However, $La_{1-x}Ba_xMnO_{3-\delta}$ derived double perovskites have been rarely studied as anodes of SOFCs by now.

In this work, $La_{0.5}Ba_{0.5}Mn_{1-x}(CoFe)_xO_{3-\delta}$ (x = 0-0.2) is studied for the first time as an anode material for SOFCs with hydrogen and methane as fuels. The phase transition and the exsolution of B-site elements during the reduction process are investigated, and the formation of the double-perovskite structure is proved. Metal-oxide nanoparticles with a core-shell structure exsolve from the

double-perovskite parent, which improve the catalytic activity of the anode significantly. The anode also shows a high stability in methane atmosphere.

2. Experimental

2.1. Preparation of Materials

$La_{0.5}Ba_{0.5}MnO_{3-\delta}$ (LBM), $La_{0.5}Ba_{0.5}Mn_{0.9}Fe_{0.05}Co_{0.05}O_{3-\delta}$ (LBMFC-1) and $La_{0.5}Ba_{0.5}Mn_{0.8}Fe_{0.1}Co_{0.1}O_{3-\delta}$ (LBMFC-2) powders were synthesized through the pechini method.[34, 38] Stoichiometric $La(NO_3)_3 \cdot 6H_2O$ (99.9%, Aladdin), $Ba(NO_3)_2$ (99.5%, Aladdin), $Mn(NO_3)_2$ solution (AR, 50 wt.% in H_2O, Aladdin), $Co(NO_3)_2 \cdot 6H_2O$ (99.99%, Aladdin) and $Fe(NO_3)_3 \cdot 9H_2O$ (99.99%, Aladdin) were dissolved in distilled water. Citric acid (99.5%, Aladdin) and ethylene glycol (Guangfu fine chemical, Ltd., China) were added into the solution as complexation agents. The concentrations of metal cations, citric acid and ethylene glycol were 0.2, 0.6 and 0.3 mol L^{-1}, respectively. The pH of the solution was kept at about 8 with the addition of ammonium hydroxide. The aqueous solution was kept at 85 °C under a continuous stir. The gel formed was slowly decomposed at 350 °C to form a black precursor, and futher grounded and calcined at 950 °C for 4 h to form aonde powders. For characterization, the powders were treated with 5% H_2-95% Ar at 850 ºC for 5 h, which were denoted as D-LBM, D-LBMFC-1 and D-LBMFC-2, respectively. The synthesis procedures of $La_{0.4}Ce_{0.6}O_{2-\delta}$ (LDC) buffer layer and $Ba_{0.5}Sr_{0.5}Co_{0.8}Fe_{0.2}O_{3-\delta}$ (BSCF) cathode powders have been introduced in previous publications.[15, 52]

2.2. Characterization

The crystal structures of the anode powders before and after reduction were investiagted at room temperature via X-ray diffraction (XRD) with a D8 Focus diffractometer (Bruker Corp., Cu-Kα radiation, 40 kV and 200 mA). Thermogravimetric analysis (TGA) of fresh samples was carried out in 5% H_2-95% Ar at a heating rate of 10 ºC min^{-1} in a NETZSCH thermal analyzer (STA, 449F3).

High-resolution transmission electron microscopy (HRTEM), high-angle annular darkfield scanning TEM (HAADF-STEM) and energy dispersive X-ray (EDX) analyses were performed using a transmission electron microscope (JEOL JEM 2100) equipped with a Schottky cold emission gun and an EDX analyzer. Hydrogen temperature programmed reduction (H_2-TPR) was performed in an Autochem II 2920 instrument (Micromerritics, USA) equipped with a thermal conductivity detector. The samples were pretreated with helium at 300 ºC for 2 h and subsequently cooled down to 50 ºC. Then H_2-TPR was performed in 10% H_2-90% Ar with a flow rate of 50 mL min^{-1} from 50 to 800 ºC at a rate of 10 ºC min^{-1}. X-ray photoelectron spectroscopy (XPS) analysis was performed using a Thermo ESCALAB 250Xi XPS imaging spectrometer. The XPS spectra were referenced to the C 1s bonding energy (284.8 eV). The surface and cross-sectional morphologies of the single cells were characterized with a scanning electron microscope (SEM, S-4800, Hitachi, Japan).

The elecrical conductivities of the samples were measured via a four-probe direct current method. The powders of LBM, LBMFC-1 and LBMFC-2 were pressed into rectangular bars and then sintered at 950 ºC in air for 12 h. The bars were reduced in 5% H_2-95% Ar at 850 ºC for 5 h. Then the electrical conductivity was measured with an electrochemical workstation (VersaSTAT 3, Ametek) in 5% H_2-95% Ar and air, respectively.

2.3. Cell Fabrication and Test

$La_{0.8}Sr_{0.2}Ga_{0.8}Mg_{0.2}O_{3-\delta}$ (LSGM) electrolyte powder (Fuel cell materials Co., USA) was pressed into pellets with a diameter of 20 mm under 200 MPa, and subsequently sintered in air at 1450 ºC for 20 h. The obtained pellet was polished to achieve a thickness of 300 μm. LBM, LBMFC-1, LBMFC-2, BSCF and LDC powders were mixed with a binder (V006, Heraeus Ltd.), respectively, to form slurries. The LDC slurry was screen-printed on the LSGM layer and sintered at 1400 ºC for 2 h to form a buffer layer.[15] The anode slurry was printed on the LDC layer, and the BSCF slurry was printed

on the other side of the electrolyte layer. The geometrical areas of the anode and cathode were both 0.5 cm^2. The pellet was finally calcined at 950 ^oC in air for 4 h. Both electrodes were coated with Ag paste as current collectors.

Before the performance test, the anode of the cell was reduced at 850 ^oC in 5% H_2-95% Ar for 2 h. The cells were tested with humidified H_2 and CH_4 (with 3% H_2O) as fuels and oxygen as oxidant. All the gases were supplied at a flow rate of 100 ml min^{-1}. The electrochemical impedance spectra (EIS) of the cells were recorded from 1 MHz to 0.1 Hz with an amplitude of 10 mV at open circuit voltage (OCV).

3. Results and Discussion

3.1. Powder Characterization

Pure LBM exhibits a mixed cubic and hexagonal perovskite phases (Fig. 1a). The hexagonal phase is attributed to the formation of $BaMnO_{3-\delta}$ (JCPDS70-3616), which is usually observed in LBM synthesized in an oxidizing atmosphere due to the perferable high oxidation state of Mn^{4+}.[44, 53-56] The Rietveld refinement of the XRD pattern of LBM is shown in Fig. S1, and the calculated lattice parameters are listed in Table S1. No phase transition is observed when Mn is partially substituted by Co and Fe.

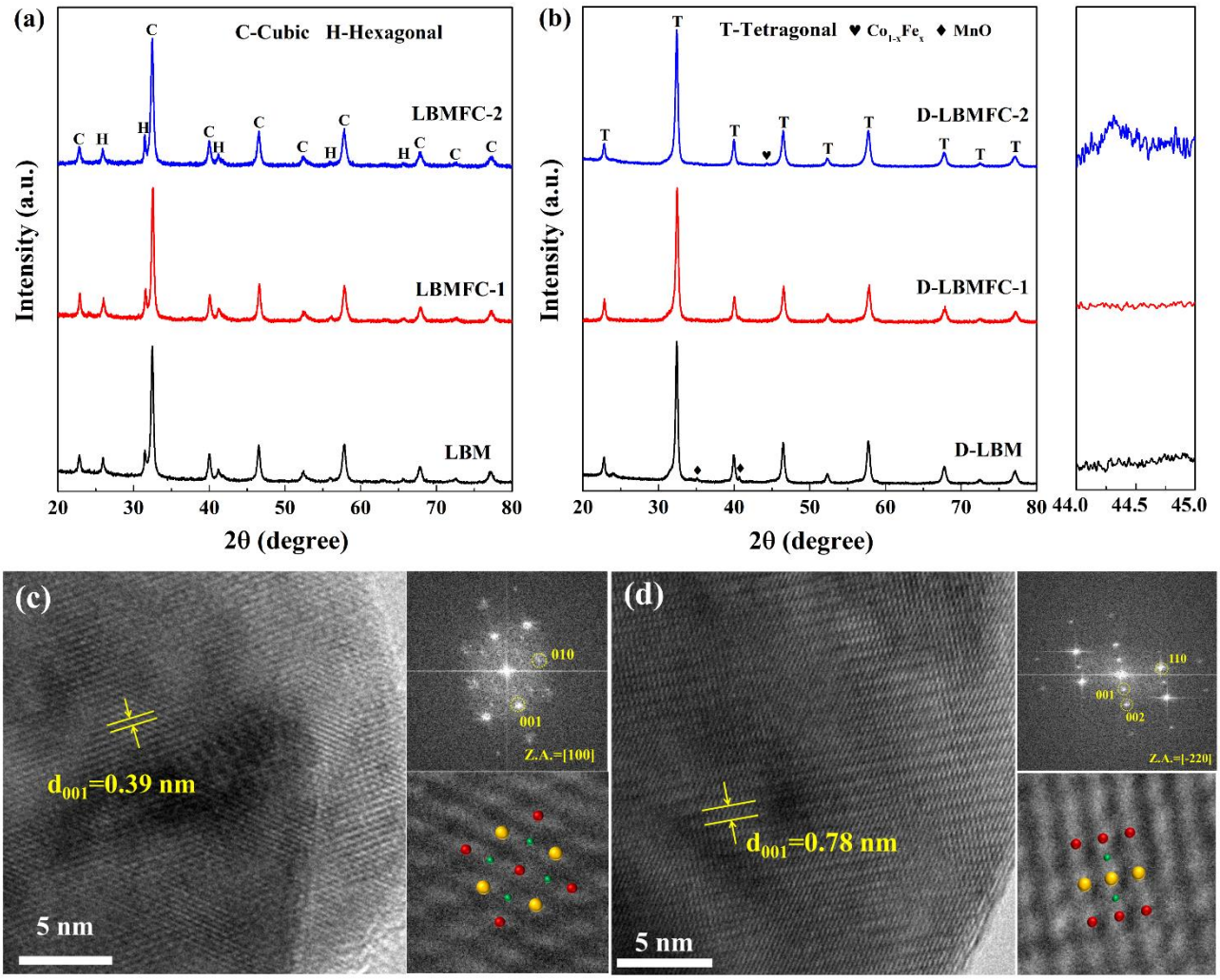

Fig. 1. XRD patterns of various anode powders (a) before and (b) after reduction. HRTEM images and corresponding FFT patterns of (c) fresh LBMFC-2 and (d) A-site ordered D-LBMFC-2 powders. The yellow, red and green spheres in the insets represent Ba, La, and Mn/Fe/Co atoms, respectively.

The hexagonal phase disappears after the LBM is reduced in 5% H_2-95% Ar at 850 °C for 5 h (Fig. 1b). The Rietveld refinement of the XRD result of D-LBM (Fig. S2) confirms a tetragonal sturcture, space group *P4/mmm* with $a = b = 3.91314$ Å and $c = 7.80974$ Å (Table S1), implying an A-site layered double-perovskite structure.[53, 56] The formation of the layered structure with the [LaO_δ-MnO_2-BaO-MnO_2-LaO_δ] series along the *c* axis and the lack of oxygen specifically in the LaO_δ layers

are due to the general preference of the smaller La^{3+} ions, which are 12-coordinated in the unreduced perovskite, to take eight-fold coordination accompanied with the loss of lattice oxygen.[54] The main structure of the anode is maintained after the doping of Fe and Co. The HRTEM image and the fast Fourier transformation (FFT) analysis result of LBMFC-2 reveal a lattice space of 0.39 nm (Fig. 1c), consistent with (0 0 1) planes of the cubic structure (space group *Pm*-3*m*) determined by the Rietveld refinement of the XRD result (Fig. S3, Table S1). The HRTEM and FFT results of D-LBMFC-2 show a lattice space of 0.78 nm (Fig. 1d), corresponding to the lattice constant of (0 0 1) planes (space group *P*4/*mmm*) along the *c* axis (Fig. S4, Table S1). Meanwhile, (0 0 2) planes along the *c* direction with a lattice space of 0.39 nm are also observed in the FFT result of D-LBMFC-2, demonstrating that D-LBMFC-2 has an A-site ordered layered perovskite sturcture.

Weak peaks corresponding to MnO phase (JCPDS75-0626) are observed in XRD pattern of D-LBM. Similar phase transition processes and exsolution of MnO are involved in the reduction of $Pr_{0.5}Ba_{0.5}MnO_{3-\delta}$ and $Nd_{0.5}Ba_{0.5}MnO_{3-\delta}$.[34, 35, 37] The partial substitution of Mn by Fe alone results in the stabilization of the perovskite structure and the suppression of the MnO segregation on the surface during the reduction, while the partial replacement of Mn by Co leads to a more serious decomposition of the perovskite structure (Fig. S5). The peaks of MnO in the XRD patterns of D-LBMFC-1 and D-LBMFC-2 are much weaker than that in D-LBM, proving that the co-doping of Co and Fe suppresses the formation of MnO during the reduction. In the XRD pattern of D-LBMFC-2, besides the characteristic peaks of the double-perovskite structure, a peak at 44.302° is also observed (the zoom-in plot), which corresponds to a lattice parameter of 3.537 Å in the *Fm*-3*m* space group of the exsolved metal (Table S1). Since the lattice parameters of metallic Co (JCPDS 89-4307) and Fe (JCPDS 88-2324) in the *Fm*-3*m* space group are 3.544 and 3.430 Å, respectively, the composition of

the nanoparticles exsolved is approximately $Co_{0.94}Fe_{0.06}$.[57] There is no noticeable peak of Co-Fe alloy in the XRD pattern of D-LBMFC-1 probably due to its low amount.

It is well known that the exsolution ability of Fe is highly influenced by cations at A and B sites in the perovskite. For instance, Fe in single perovskite oxides such as $La_{1-x}Sr_xFeO_{3-\delta}$ is liable to be reduced, resulting in the decomposition of the perovskite structure.[58] On the other hand, Fe cannot exsolve from double perovskites such as $PrBaMn_{1.7}Fe_{0.3}O_{5+\delta}$[36] and $PrBa(Fe_{0.8}Sc_{0.2})_2O_{5+\delta}$[59] during reduction. The density functional calculation results also reveal that the co-segregation energy of Fe-$V_O^{\cdot\cdot}$ is higher than those of Co-$V_O^{\cdot\cdot}$ and Mn-$V_O^{\cdot\cdot}$ in the doped $PrBaMn_2O_{5+\delta}$, which hinders the exsolution of metallic Fe nanoparticles on the surface.[36] However, the co-exsolution of $Co_{1-x}Fe_x$ and $Ni_{1-x}Fe_x$ alloys have been reported from a number of perovskites such as $(La_{0.7}Sr_{0.3})(Cr_{0.85}Ni_{0.1125}Fe_{0.0375})O_{3-x}$,[60] $Pr_{0.4}Sr_{0.4}Co_{0.2}Fe_{0.7}Nb_{0.1}O_{3-\delta}$[27] and $Sr_2FeMo_{0.65}Ni_{0.35}O_{6-\delta}$.[25] Since Co is more reducible than Fe, the atom ratio of Co:Fe in the exsolved alloy is much higher than that in the bulk perovskite in most cases.[27, 31, 61] A further increase of the substitute degree, e.g. $La_{0.5}Ba_{0.5}Mn_{0.7}Fe_{0.15}Co_{0.15}O_{3-\delta}$ (LBMFC-3), brings about the destruction of the perovskite structure (Fig. S6).

The TGA results reveal the phase transition and the loss of lattice oxygen processes in various samples during the reduction (Fig. 2). In order to eliminate the interference of adsorbed water, the TGA curves all start from 250 °C.[38, 39] The quick decrease of the weight between 300 and 500 °C (Stage 1) indicates the rapid formation of oxygen vacancy accompanied with the phase change. At the same temperature, the loss of weight increases with the increase of incorporating amount, indicating that the doping increases the lability of oxygen in the perovskite. The following decrease in weight at a much lower rate between 500 and 750 °C (Stage 2) corresponds to the partial removal of lattice oxygen atoms strongly bonded with the cations in the perovskite. Sengodan et al.[34] observed

a similar weight loss process during the reduction of $Pr_{0.5}Ba_{0.5}MnO_3$ between 400-800 °C and demonstrated the phase change and the formation of the layered perovskite structure by *in situ* XRD test. Further increase of the temperature leads to a weight loss at a high rate (Stage 3), which is attributed to the loss of oxygen atoms bonded with B site cations, resulting in the co-segregation and exsolution of MnO and Co-Fe alloy on the surface as shown in the XRD results.[36, 39] A slow weight decrease followed by a quasi-stable state is observed during the prolonged reduction process at 850 °C for 5 h (Stage 4), indicating a completion of reduction and exsolution.[39] The weight loss increases with the rise of the substitute degree, implying more oxygen vacancies and exsolved metallic particles. Besides, the weight loss of Fe-doped LBM is similar to that of pure LBM and much lower than that of Co-doped LBM (Fig. S7), further confirming the higher reduction stability of Fe than that of Co, which is consistent with the XRD results (Fig. 1 and Fig. S5).

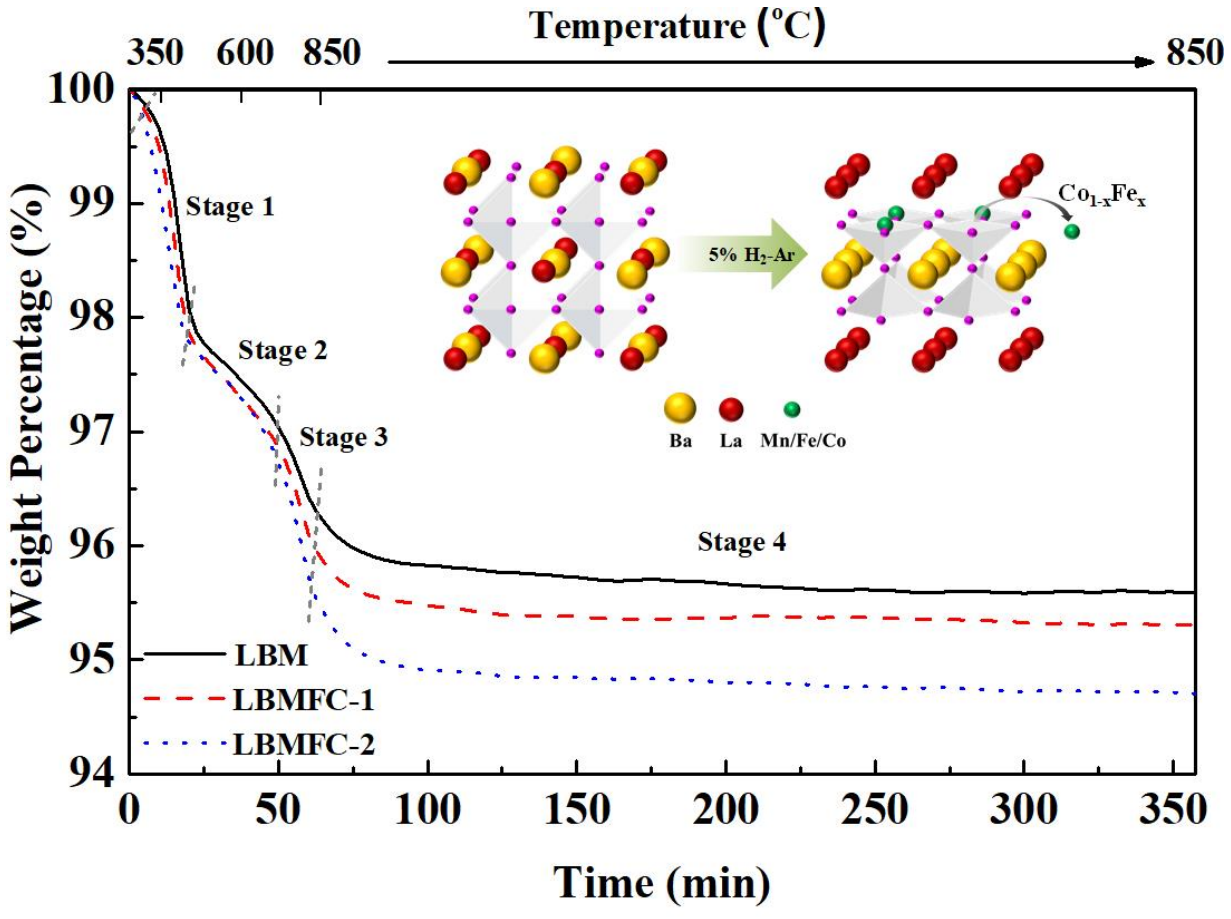

Fig. 2. TGA results of various samples in 5% H_2-95% Ar.

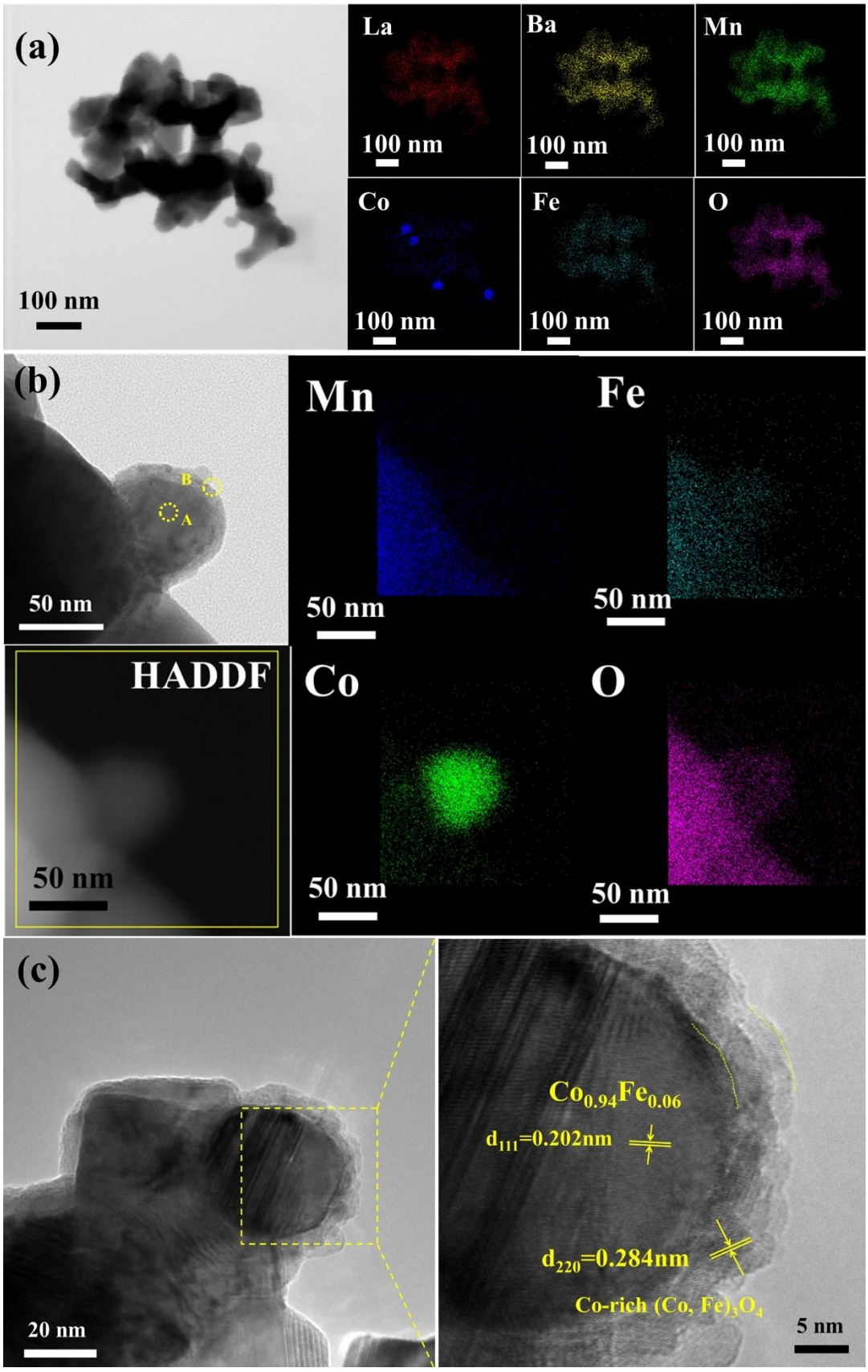
(a)
100 nm
La
100 nm
Ba
100 nm
Mn
100 nm
Co
100 nm
Fe
100 nm
O
100 nm
(b)
B
A
50 nm
Mn
50 nm
Fe
50 nm
HADDF
50 nm
Co
50 nm
O
50 nm
(c)
20 nm
$Co_{0.94}Fe_{0.06}$
d_{111}=0.202nm
d_{220}=0.284nm
Co-rich $(Co, Fe)_3O_4$
5 nm

Fig. 3. Images of D-LBMFC-2 powder. (a) STEM image and the corresponding EDX elemental mappings; (b) TEM and HAADF-STEM images of exsolved nanoparticles with corresponding EDX elemental mapping profile and (c) HRTEM image of an exsolved nanoparticle.

The STEM image with the EDX elemental mapping of D-LBMDC-2 is shown in Fig. 3a. La, Ba, Mn, Fe and O all distribute homogeneously, while the segregation of Co is observed clearly. The HRTEM image of the Co-enriched area in D-LBMFC-2 shows the exsolution of nanoparticles with a core-shell structure, which are partially embedded in the parent perovskite (Fig. 3b). The HAADF-STEM images coupled with EDX element mapping confirm the uniform distribution of Mn, Fe and O in the parent pervoskite, while the concentration of Co near the surface of the perovskite is negligible, indicating that most of surface Co cations are reduced and exsolved. The atom ratios of Co:Fe:O are 0.785:0.078:0.137 in the center (Area A) and 0.455:0.030:0.515 at the edge (Area B) of the exsolved nanoparticle, which are calculated based on the EDX elemental mapping results. The ratio between Co and Fe is approximately 0.94:0.06, which is in accordance with the XRD result. A more obvious core-shell sturcture of the exsolved nanoparticle is shown in Fig. 3c. The diameter of the core is 30-40 nm, and the thickness of the shell is about 5 nm. The interplanar spacing of 0.202 nm of the core corresponds to the (1 1 1) crystal planes of $Co_{0.94}Fe_{0.06}$ alloy, while the spacing of 0.284 nm of the shell is consistent with the (2 2 0) planes of Co-rich $(Co, Fe)_3O_4$. Therefore, the exsolved nanoparticles should exhibit a metal-oxide core-shell structure, and the oxygen in the center of the EDX element mapping profile can be explained by the two-dimensional feature of the TEM result.

The core-shell structure of the exsolved $Co_{1-x}Fe_x$ and $Co_{1-x}Ni_x$ particles have been observed in many research works.[27, 36, 62] However, the formation mechanism of the oxide shell has not been well

explained. Bulk CoO is not thermodynamically stable at 850 ºC when the P_{O2} is lower than 10^{-16} atm. Nonetheless, the reduction of CoO_x nanoparticles is highly influenced by the supporter. Generally, CoO_x particles which interact strongly with the supporter are less reducible.[63-65] Meanwhile, the smaller Co particles with more surface contact with the support have a lower reducibility. Therefore, the existence of the oxide shell in the 5% H_2-95% Ar ($P_{O2} \sim 10^{-23}$-10^{-24} atm at 850 ºC) is reasonable since the exsolved nanoparticles interact strongly with the perovskite supporter. To further verify this idea, LBMFC-2 was reduced in a less reductive 97% H_2-3% H_2O atmosphere ($P_{O2} \sim 10^{-21}$ atm at 850 ºC), and the thickness of the oxide shell increases to about 10 nm (Fig. S8). The thickness of the shell is closely related to the partial pressure of O_2 in the reducing atmosphere, confirming that it is formed during the reduction process.

Fig. S9 shows H_2-TPR profiles of LBM and LBMFC-2 powders. LBM presents a hydrogen consumption peak at around 365 ºC. With the doping of Fe and Co, the hydrogen consumption peak shifts to a lower temperature at about 349 ºC, implying a reduced metal-oxygen bond energy in the perovskite due to the higher electronegativities of Fe (1.83) and Co (1.88) than that of Mn (1.55),[66] which is in accordance with the TGA results (Fig. 2). The reduction temperatures of the anode materials are much lower than those of doped and undoped $Pr_{0.5}Ba_{0.5}MnO_{3-\delta}$.[38] The lower reduction temperature indicates more labile oxygen, which is expected to modify the redox capacity and facilitate the formation of oxygen vacancies. That is further proved by the O 1s XPS results (Fig. S10 and Table S2). With the increase of Fe and Co in the reduced samples, the content of lattice oxygen decreases, while that of adsorbed oxygen species rises. The surface oxygen species are mainly adsorbed on the oxygen vacancies and would be desorbed easily at an elevated temperature.[67, 68] Therefore, a high content of adsorbed oxygen species reflects a large number of oxygen vacancies,

which brings about a high oxygen ionic conductivity and thus accelerates the electrochemical oxidation of the fuels.

3.2. Electrical Conductivity

The conductivities of D-LBM sintered at 950 °C are 5.70 and 0.88 S cm^{-1} at 850 °C in air and 5% H_2-95% Ar, respectively (Fig. S11). With the increase of the doping content of Co and Fe, the conductivity of the sample reduces slightly. It is well known that the oxidation of Mn^{3+} to Mn^{4+} is the main origin of the electronic conductivity of manganate perovskites.[69] The content of Mn^{4+} in the reduced samples decreases with the increase of Co and Fe (Fig. S12 and Table S3), resulting in a decline of the conductivity. The exsolved $Co_{0.94}Fe_{0.06}$ nanoparticles do not contribute much to the conductivity owing to their low content and high dispersion (Fig. 3a), thus not forming a continuous conductive network.

3.3. SOFC Performance

Fig. S13 shows the surface and cross-sectional microstructures of a single cell with the LBMFC-2 anode. The anode layer possesses a porous structure, which provides sufficient channels and surface for the diffusion and adsorption of fuels.[70] A good connection between the porous anode layer, the porous LDC interlayer and the dense LSGM electrolyte layer is formed, which would result in a low interfacial resistance. The thicknesses of the LBMFC-2 and LDC layers are 35-36 and 10-11 μm, respectively.

Fig. 4a exhibits *I-V* and *I-P* characteristics of the single cells with various anodes fed with wet H_2 (~3% H_2O) at 850 °C. The OCVs of the cells are around 1.0-1.1 V. The P_{max} of 962, 1241 and 1479 mW cm^{-2} are achieved by the cells with D-LBM, D-LBMFC-1 and D-LBMFC-2 as the anodes, respectively. The high P_{max} of the cell with D-LBMFC-2 anode is attributed to the high catalytic activity of the anode with more active sites of nanoparticles exsolved on its surface. Meanwhile, more

oxygen vacancies and labile oxygen in the perovskite brought by the doping of Co and Fe is another reason for the improved catalytic activity of the anode, which is demonstrated by the XPS and H_2-TPR results. However, the cell with D-LBMFC-3 anode shows a P_{max} of 1272 mW cm^{-2} (Fig. S14), lower than that of the cell with D-LBMFC-2 anode due to the the decomposition of the anode (Fig. S6). The P_{max} of the cell increases with the increase of the operating temperature. The cell with the D-LBMFC-2 anode exhibits P_{max} of 210, 383, 653, 970 and 1479 mW cm^{-2} with wet H_2 as fuel at 650, 700, 750, 800 and 850 °C, respectively (Fig. 4b). The performances of the cells in this work are among the best in those of the cells with a perovskite anode and a similar congfiguration using H_2 as fuel (Fig. 4c and Table S4).

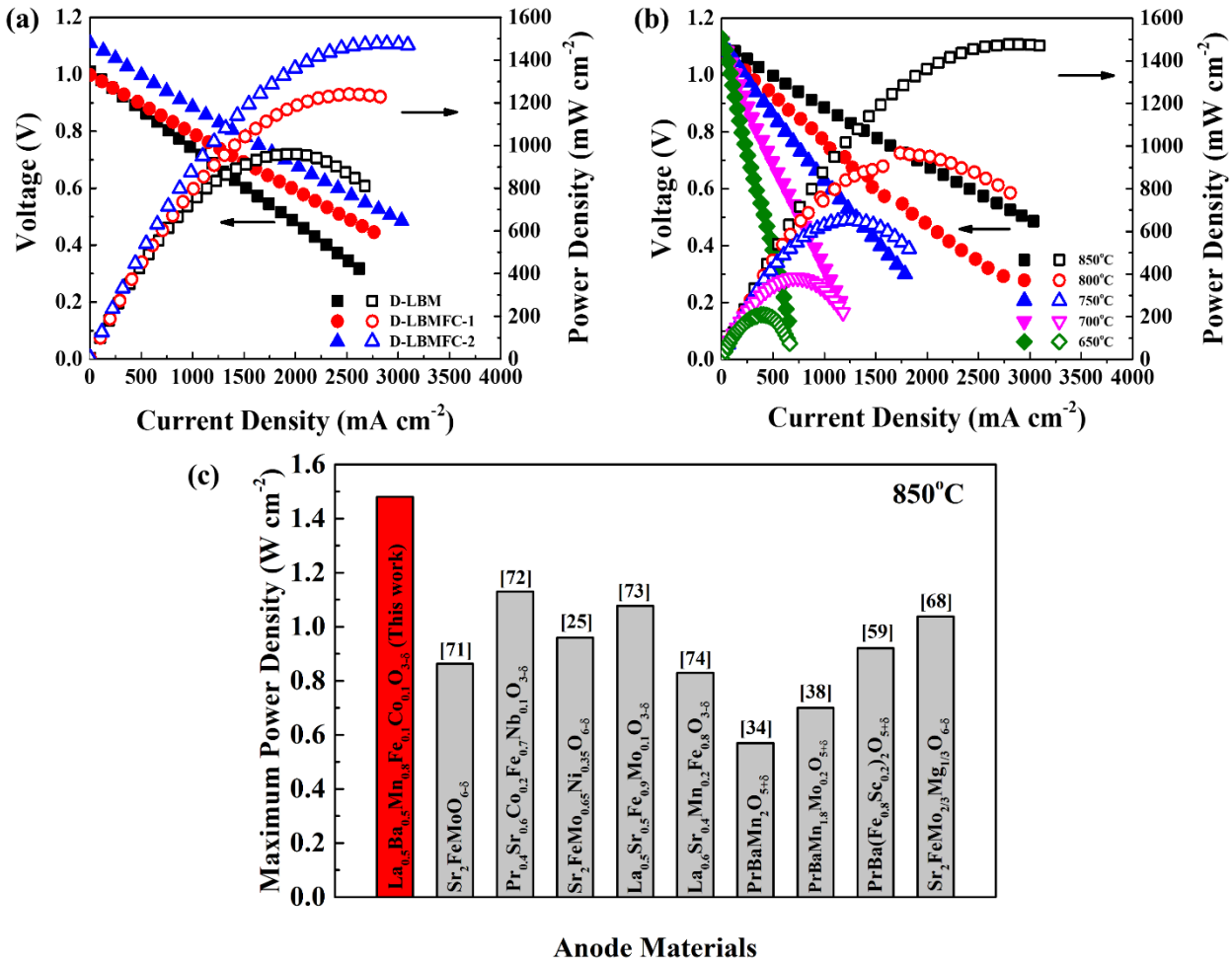

Fig. 4. *I-V* and *I-P* curves of (a) single cells with different anodes at 850 ºC and (b) single cell with D-LBMFC-2 anode at various temperatures with wet H_2 as fuel; (c) Comparison of the P_{max} of single cells with various high-performance anodes at 850 ºC.[25, 34, 38, 59, 68, 71-74] All of the anode layers in (c) were screen-printed on the electrolyte layers. The thicknesses of the anode layers were generally 30-40 μm, which were sintered at 950-1050 ºC.

When the fuel is switched to wet CH_4 (~3% H_2O), the OCVs of the cells decrease to 0.85-0.95 V at 850 ºC (Fig. 5a) because the electrooxidation of CH_4 is much more difficult than that of H_2.[75] The P_{max} of the cells with D-LBM, D-LBMFC-1 and D-LBMFC-2 as anodes at 850 °C are 226, 389 and 503 mW cm^{-2}, respectively. Fig. 5b provides EIS of various cells at 850 ºC. The intercepts of the semicircles at high frequency regions on the real axis are usually associated with the ohmic resistances and the arcs are attributed to the polarization of the electrodes. The ohmic resistances of all the cells are almost the same since the electric conductivities of the anodes are similar (Fig. S11), while as for polarization resistances, an order of D-LBM > D-LBMFC-1 > D-LBMFC-2 is observed, indicating an improvement of the catalytic activity of the anode towards the electrochemical oxidation of CH_4. With a further increase of the substite degree of the anode, the P_{max} of the cell with D-LBMFC-3 anode decreases to 287 mW cm^{-2} (Fig. S14).

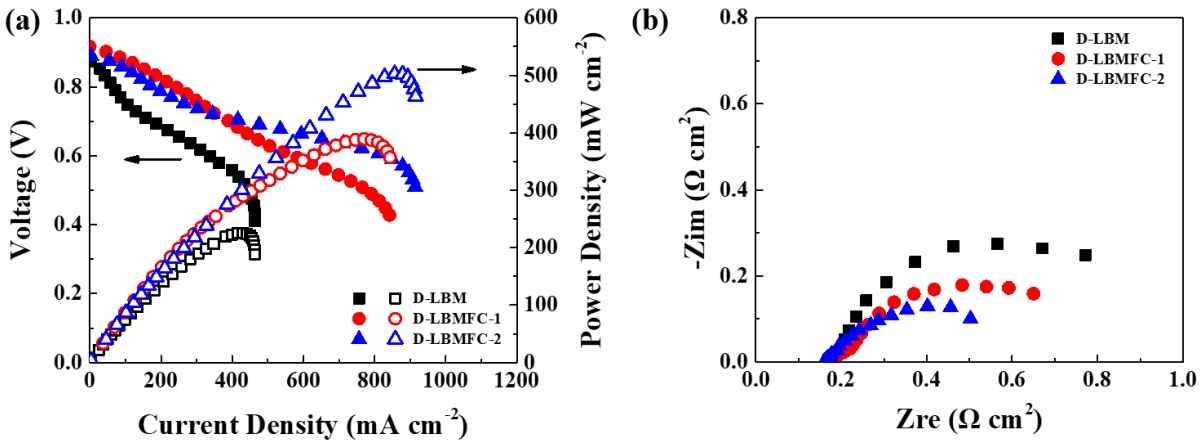

Fig. 5. (a) *I-V* and *I-P* curves and (b) electrochemical impedance spectra of single cells with various anodes at 850 °C with wet CH_4 as the fuel.

3.4. Effects of different components of anode

3.4.1. Double-perovskite bulk phase

The cell with D-LBMFC-2 anode exhibits the highest performance in 750-850 °C with both H_2 and CH_4 fuels (Fig. S15). In order to investigate the effects of each component on the performance of the anode, comparative tests are performed subsequently. Since nearly all of the Fe remains in the parent perovskite while most of the surface Co exsolves (Fig. 3b and Fig. S8), $La_{0.5}Ba_{0.5}Mn_{0.9}Fe_{0.1}O_{3-\delta}$ (LBMF-1) and $La_{0.5}Ba_{0.5}Mn_{0.8}Fe_{0.2}O_{3-\delta}$ (LBMF-2) were synthesized as anode materials for comparison. The SEM results confirm that no obvious nanoparticle is exsolved on the surface of D-LBMF-2 after reduction (Fig. S16). As shown in Fig. 6, the P_{max} of the cell with D-LBMF-1 anode reaches 1096 and 277 mW cm^{-2} at 850 °C with wet H_2 and wet CH_4 as the fuels, respectively, which are higher than those of the cell with D-LBM anode. As mentioned above, the doping of Fe brings about more oxygen vacancies and labile oxygen in the perovskite, resulting in a higher catalytic activity. The P_{max} is further improved when D-LBMF-2 is used as the anode. It should be mentioned that D-LBMF-1 is not exactly the same as the bulk perovskite of D-LBMFC-2 since Co in the latter

is not entirely exsolved during the reduction. Nonetheless, the results prove that Fe in D-LBM facilitates the electrochemical oxidation of H_2 and CH_4.

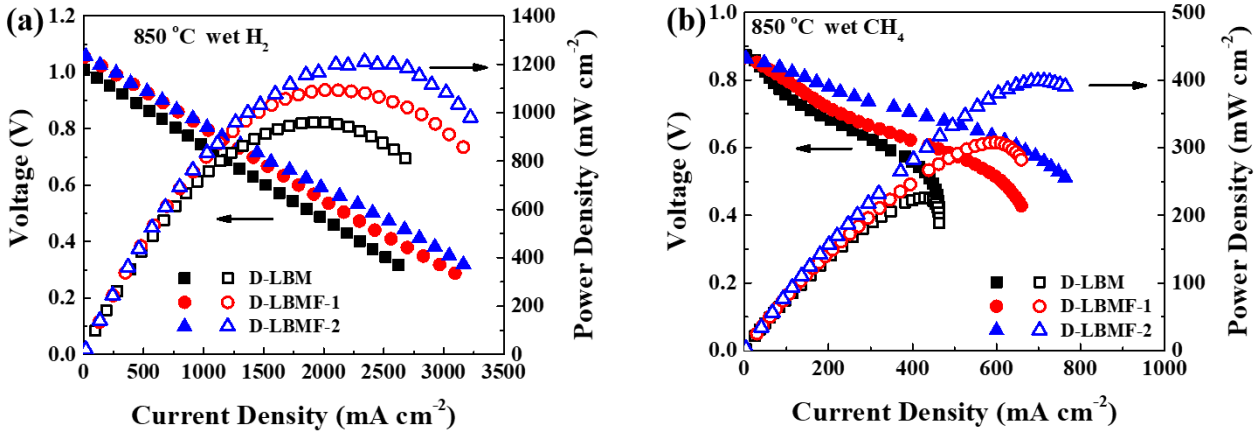

Fig. 6. *I-V* and *I-P* curves of single cells with various amounts of Fe in anodes at 850 °C fed with (a) wet H_2 and (b) wet CH_4.

3.4.2. Metal-oxide core-shell nanoparticles

To study the effect of the exsolved metal-oxide core-shell nanoparticles on the performance of the D-LBMFC-2 anode, equivalent Co (about 2.4 wt%) is added into LBMF-1 through infiltration to form D-LBMF-1/Co for comparison. The infiltration process is introduced in the supporting information (Fig. S17). Unlike the *in situ* exsolved nanoparticles with a core-shell structure, no oxide shell is observed after reduction on the infiltrated particles which adhere to the perovskite more smoothly compared with the exsolved nanoparticles (Fig. S18). It further proves that the oxide shell on the exsolved nanoparticle is formed during reduction, not re-oxidation when exposed to air at room temperature before characterization. As mentioned above, the exsolved nanoparticles partially embedded in the perovskite shows a stronger metal-support interaction than the infiltrated nanoparticles. Therefore, the infiltrated nanoparticles are more reducible. Meanwhile, it is very interesting that $Co_{1-x}Fe_x$ alloy is formed on the surface of the perovskite (Fig. S18) though only Co is

added through infiltration, indicating the exsolution of Fe during the reduction. In contrast, no Fe is exsolved from D-LBMF-2 without the infiltration of Co (Fig. S16), implying that Co facilitates the exsolution of Fe which is worth further study.

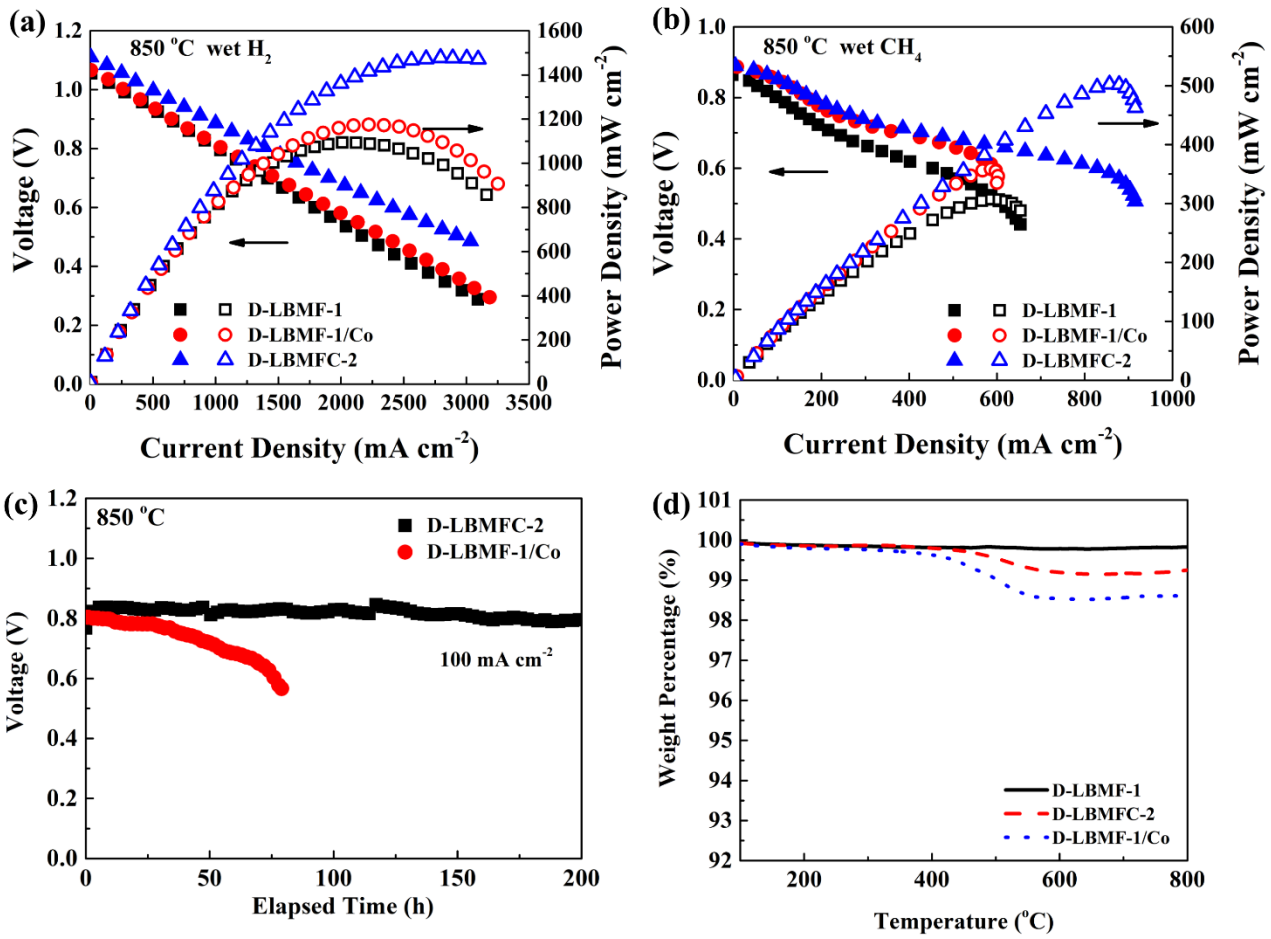

Fig. 7. *I-V* and *I-P* curves of single cells with various anodes fed with (a) wet H_2 and (b) wet CH_4; (c) Chronopotentiometry results of single cells with D-LBMFC-2 and D-LBMF-1/Co anodes fed with wet CH_4 at 850 °C; (d) TGA curves of various anodes after carbon deposition in wet CH_4.

Compared to the cell with D-LBMF-1 anode, the cell with the infiltrated anode exhibits high performances with both H_2 and CH_4 fuels attributed to the additional catalytic function of metallic nanoparticles (Fig. 7). Nonetheless, though the amount of the metal catalyst added through infiltration should be higher than that on the surface of D-LBMFC-2 because of the incomplete exsolution in the

latter anode, the catalytic activity of the infiltrated anode is lower than that of the anode containing exsolved nanoparticles, which is partially due to the sintering of the infiltrated particles at the operating temperature.[39, 76] Meanwhile, it has been reported that Co-CoO_x core-shell nanoparticles are an excellent catalyst for hydrocarbon oxidation.[77, 78]

The cell with D-LBMFC-2 anode is tested with wet CH_4 as the fuel at 850 ºC under an output current density of 100 mA cm^{-2} for 200 h without obvious degradation (Fig. 7c). Compared with other excellent perovskite anode materials reported previously, D-LBMFC-2 shows a first-rate activity and a superior stability with CH_4 as the fuel (Table 1). No carbon is observed on the surface of the anode after the test (Fig. S19). In contrast, the performance of the cell with D-LBMFC-1/Co anode drops quickly during the first 60 h, which is mainly due to carbon deposition on the infiltrated anode. In order to study the coking resistance of the anodes, the powders were treated in wet CH_4 at 850 ºC for 5 h, and then the amount of carbon deposited were measured through TGA in air. As shown in Fig. 7d, the weight loss of D-LBMFC-2 and D-LBMF-1/Co above 400 ºC could be attributed to the oxidation of carbon. D-LBMF-1 shows the highest resistance to carbon deposition. The weight loss of D-LBMFC-2 and D-LBMF-1/Co are about 0.8 wt.% and 1.5 wt.%, respectively. Fig. 8 shows the morphology of D-LBMFC-2 and D-LBMF-1/Co powders after carbon deposition. No obvious carbon deposit is observed on the exsolved core-shell particles in D-LBMFC-2 (Fig. 8 a, b). On the contrary, the infiltrated nanoparticle in D-LBMF-1/Co is covered by a carbon layer with an average thinkness of about 10 nm (Fig. 8 c, d). The carbon shows a well-ordered structure, indicating a high degree of crystallinity which is difficult to be removed by oxidation. Though Co shows a high catalytic activity for carbon deposition,[6] the oxide shell covering the exsolved nanoparticles improves the resistance to coking of the anode.[78, 79] Meanwhile, the exsolved nanoparticles are partially embedded in the parent perovskite (Fig. 3c). The strong metal-support interaction provides a promising thermal stability and

a high resistance to carbon deposition of the anode.[24, 36, 80-82] On the contrary, the infiltrated $Co_{1-x}Fe_x$ nanoparticles with a weaker interaction with the perovskite trend to agglomerate at a high temperature, which might be another reason for the rapid performance degradation of the single cell.

Table 1. P_{max} and stability of single cells with high-performance perovskite anodes fed with CH_4.

Anode	Electrolyte	Electrolyte Thickness (μm)	T (°C)	P_{max} (W cm^{-2})	Test period	Ref
$Sr_2MgMoO_{6-\delta}$	LSGM-1[a)]	300	800	0.44	50 cycles	[15, 83]
Sr_2CoMoO_6	LSGM-1	300	800	0.527	50 cycles	[84]
$Sr_2FeMoO_{6-\delta}$	LSGM-1	300	850	0.6	20 cycles	[71]
$Pr_{0.8}Sr_{1.2}(Co,Fe)_{0.8}Nb_{0.2}O_{4+\delta}$	LSGM-1	300	850	0.6	~150 h (800 °C)	[28]
$Sr_2FeNb_{0.2}Mo_{0.8}O_{6-\delta}$	LSGM-2[b)]	200	800	0.38	200 h (700 °C)	[85]
$Sr_2FeMo_{0.65}Ni_{0.35}O_{6-\delta}$	LSGM-3[c)]	300	850	0.5	24 h (750 °C)	[25]
$La_{0.5}Sr_{0.5}Fe_{0.9}Mo_{0.1}O_{3-\delta}$	LSGM-2	280	850	0.769	100 cycles (700 °C)	[73]
$(PrBa)_{0.95}(Fe_{0.9}Mo_{0.1})_2O_{5+\delta}$	LSGM-2	200	800	0.54	420 h (750 °C)	[86]
$PrBaMn_2O_{5+\delta}$ with PBM	LSGM-2	300	850	0.25	-	[34]
$PrBaMn_2O_{5+\delta}$ with 15 wt% Co–Fe	LSGM-2	300	850	0.57	-	
$PrBaMn_{1.8}Mo_{0.2}O_{5+\delta}$	YSZ[d)]	100	850	0.6	-	[38]
$PrBaMn_{1.5}Fe_{0.5}O_{5+\delta}$	LSGM-1	520	850	0.34	~100 h (750 °C)	[40]
$Sr_2FeMo_{2/3}Mg_{1/3}O_6$	LSGM-3	300	900	0.12	~100 h (850 °C)	[68]
$La_{0.5}Ba_{0.5}Mn_{0.8}Fe_{0.1}Co_{0.1}O_{3-\delta}$	LSGM-3	300	850	0.5*	200 h	This work

[a)]LSGM-1: $La_{0.8}Sr_{0.2}Ga_{0.83}Mg_{0.17}O_{2.815}$;
[b)]LSGM-2: $La_{0.9}Sr_{0.1}Ga_{0.8}Mg_{0.2}O_{3-\delta}$;
[c)]LSGM-3: $La_{0.8}Sr_{0.2}Ga_{0.8}Mg_{0.2}O_{3-\delta}$;
[d)]YSZ: yttria-stabilized zirconia.
* With pure oxygen as the cathode gas

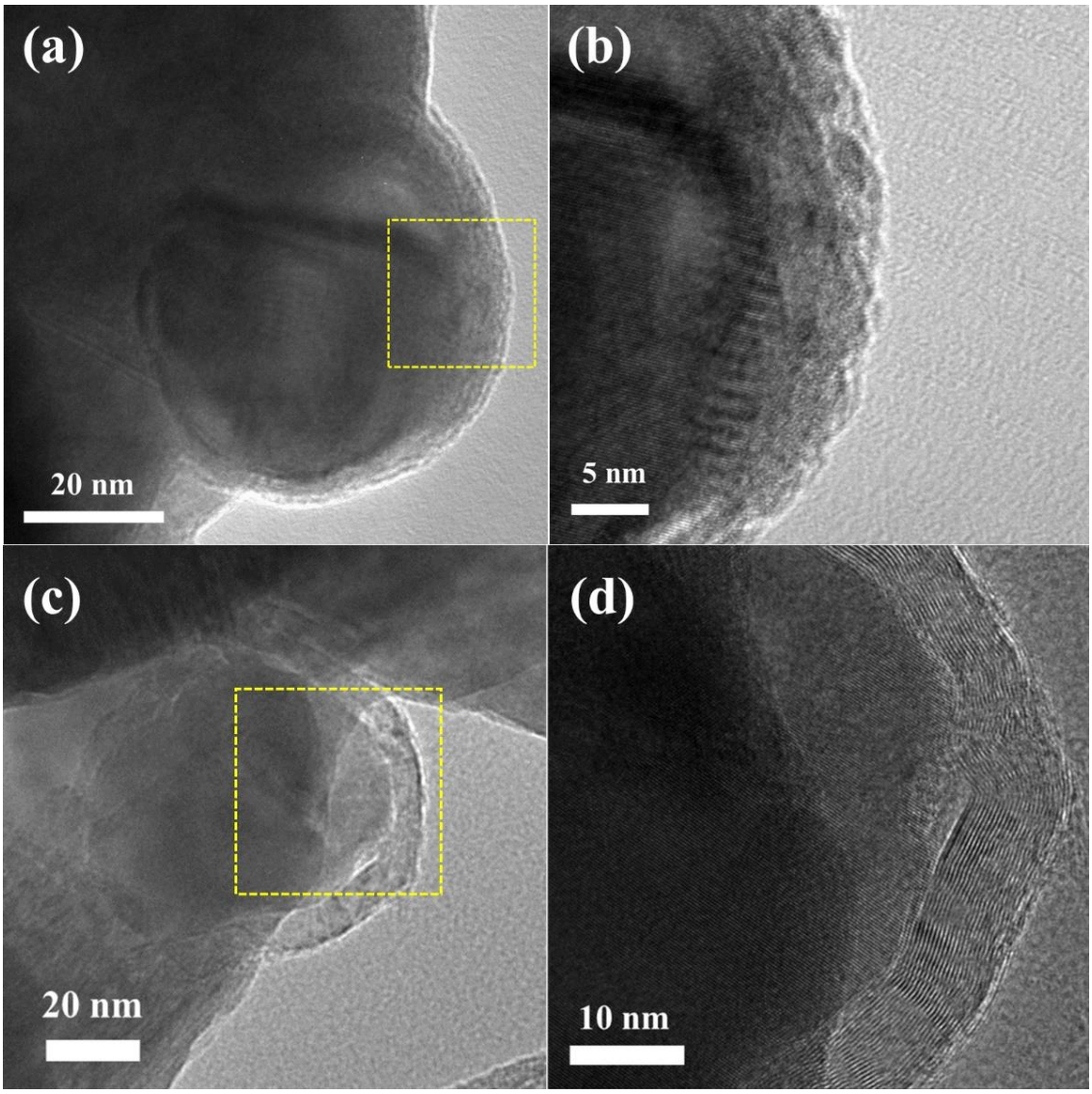

Fig. 8. TEM images of different anode powders after carbon deposition in wet CH_4. (a) D-LBMFC-2; (b) partially magnified image of (a); (c) D-LBMF-1/Co and (d) partially magnified image of (c).

4. Conclusion

In this work, a simple *in situ* strategy is developed toward efficient, stable and nonprecious metal containing composite electrocatalysts for SOFCs. Co and Fe are co-doped into the B sites of $La_{0.5}Ba_{0.5}MnO_{3-\delta}$ perovskite which exhibits a cubic-hexagonal mixed structure. An A-site ordered double-perovskite main structure is formed after reduction. During the reduction, Co and Fe exsolve from the bulk phase, and metal-oxide core-shell nanoparticles with an average size of about 50 nm are formed on the surface of the perovskite. The nanoparticles distributed homogeneously on the

surface enhance the catalytic activity of the anode significantly. Meanwhile, the incorporation of Co and Fe introduces more oxygen vacancies into the perovskite, which also accelerates the anodic kenitics. The P_{max} of the single cell with D-LBMFC-2 anode and 300 μm-thick LSGM electrolyte reaches 210, 383, 653, 970 and 1479 mW cm^{-2} with wet H_2 as the fuel at 650, 700, 750, 800 and 850 ^oC, respectively, outperforming the single cells with similar configurations. The same cell fed with wet methane exhibits a P_{max} of 503 mW cm^{-2} at 850 ^oC. Furthermore, the nanoparticles covered by an oxide shell and anchoring firmly on the perovskite exhibit a high stability. The cell displays a stable power output at 850 ^oC for 200 h with wet methane as the fuel.

Acknowledgements

The financial support of NSF of China under contract number 51402210 and the support of Tianjin Municipal Science and Technology Commission under contract number 15JCQNJC06500 are gratefully acknowledged. The work has been also supported by the Program of Introducing Talents to the University Disciplines under file number B06006, and the Program for Changjiang Scholars and Innovative Research Teams in Universities under file number IRT 0641.

Supporting Information. Rietveld refinement of the XRD patterns, characterization of LBM powders doped with Co or Fe, H_2-TPR, XPS, electrical conductivity, SEM micrographs of the single cell, the preparation procedure and characterization of the infiltrated anode.

References

1. McIntosh, S.; Gorte, R. J. Direct Hydrocarbon Solid Oxide Fuel Cells. *Chem. Rev.* **2004,** 104 (50), 4845-4865.

2. Ge, X.-M.; Chan, S.-H.; Liu, Q.-L.; Sun, Q. Solid Oxide Fuel Cell Anode Materials for Direct Hydrocarbon Utilization. *Adv. Energy Mater.* **2012,** 2 (10), 1156-1181.

3. Wang, W.; Su, C.; Wu, Y.; Ran, R.; Shao, Z. Progress in Solid Oxide Fuel Cells with Nickel-Based Anodes Operating on Methane and Related Fuels. *Chem. Rev.* **2013,** 113 (10), 8104-8151.

4. Liang, Z.; Li, T.; Kim, M.; Asthagiri, A.; Weaver, J. F. Low-Temperature Activation of Methane on the IrO_2 (110) Surface. *Science* **2017,** 356 (6335), 299-303.

5. Goodenough, J. B.; Huang, Y.-H. Alternative Anode Materials for Solid Oxide Fuel Cells. *J. Power Sources* **2007,** 173 (1), 1-10.

6. Zhang, Y.; Smith, K. J. Carbon Formation Thresholds and Catalyst Deactivation During CH_4 Decomposition on Supported Co and Ni Catalysts. *Catal. Lett.* **2004,** 95 (1), 7-12.

7. Gür, T. M. Comprehensive Review of Methane Conversion in Solid Oxide Fuel Cells: Prospects for Efficient Electricity Generation from Natural Gas. *Prog. Energy Combust. Sci.* **2016,** 54, 1-64.

8. Gross, M. D.; Vohs, J. M.; Gorte, R. J. Recent Progress in SOFC Anodes for Direct Utilization of Hydrocarbons. *J. Mater. Chem.* **2007,** 17 (30), 3071-3077.

9. Zhan, Z.; Barnett, S. A. An Octane-Fueled Solid Oxide Fuel Cell. *Science* **2005,** 308 (5723), 844-847.

10. Boldrin, P.; Ruiz-Trejo, E.; Mermelstein, J.; Bermudez Menendez, J. M.; Rami Rez Reina, T.; Brandon, N. P. Strategies for Carbon and Sulfur Tolerant Solid Oxide Fuel Cell Materials, Incorporating Lessons from Heterogeneous Catalysis. *Chem. Rev.* **2016,** 116 (22), 13633-13684.

11. Park, J.-S.; Hasson, I. D.; Gross, M. D.; Chen, C.; Vohs, J. M.; Gorte, R. J. A High-Performance Solid Oxide Fuel Cell Anode Based on Lanthanum Strontium Vanadate. *J. Power Sources* **2011,** 196 (18), 7488-7494.

12. Aguilar, L.; Zha, S.; Cheng, Z.; Winnick, J.; Liu, M. A Solid Oxide Fuel Cell Operating on Hydrogen Sulfide (H_2S) and Sulfur-Containing Fuels. *J. Power Sources* **2004,** 135 (1), 17-24.

13. Marina, O. A.; Canfield, N. L.; Stevenson, J. W. Thermal, Electrical, and Electrocatalytical Properties of Lanthanum-Doped Strontium Titanate. *Solid State Ionics* **2002,** 149 (1), 21-28.

14. Tao, S.; Irvine, J. T. A Redox-Stable Efficient Anode for Solid-Oxide Fuel Cells. *Nat. Mater.* **2003,** 2 (5), 320-323.

15. Huang, Y. H.; Dass, R. I.; Xing, Z. L.; Goodenough, J. B. Double Perovskites as Anode Materials for Solid-Oxide Fuel Cells. *Science* **2006,** 37 (28), 254-257.

16. Cowin, P. I.; Petit, C. T. G.; Lan, R.; Irvine, J. T. S.; Tao, S. Recent Progress in the Development of Anode Materials for Solid Oxide Fuel Cells. *Adv. Energy Mater.* **2011,** 1 (3), 314-332.

17. Nishihata, Y.; Mizuki, J.; Akao, T.; Tanaka, H.; Uenishi, M.; Kimura, M.; Okamoto, T.; Hamada, N. Self-Regeneration of a Pd-Perovskite Catalyst for Automotive Emissions Control. *Nature* **2002,** 418 (6894), 164-167.

18. Tanaka, H.; Uenishi, M.; Taniguchi, M.; Tan, I.; Narita, K.; Kimura, M.; Kaneko, K.; Nishihata, Y.; Mizuki, J. The Intelligent Catalyst Having the Self-Regenerative Function of Pd, Rh and Pt for Automotive Emissions Control. *Catal. Today* **2006,** 117 (1-3), 321-328.

19. Madsen, B.; Kobsiriphat, W.; Wang, Y.; Marks, L.; Barnett, S. Nucleation of Nanometer-Scale Electrocatalyst Particles in Solid Oxide Fuel Cell Anodes. *J. Power Sources* **2007,** 166 (1), 64-67.

20. Kobsiriphat, W.; Madsen, B. D.; Wang, Y.; Marks, L. D.; Barnett, S. A. $La_{0.8}Sr_{0.2}Cr_{1-x}Ru_xO_{3-\delta}$–$Gd_{0.1}Ce_{0.9}O_{1.95}$ Solid Oxide Fuel Cell Anodes: Ru Precipitation and Electrochemical Performance. *Solid State Ionics* **2009,** 180 (2-3), 257-264.

21. Tanaka, H.; Taniguchi, M.; Uenishi, M.; Kajita, N.; Tan, I.; Nishihata, Y.; Mizuki, J.; Narita, K.; Kimura, M.; Kaneko, K. Self-Regenerating Rh- and Pt-Based Perovskite Catalysts for Automotive-Emissions Control. *Angew. Chem. Int. Ed. Engl.* **2006,** 45 (36), 5998-6002.

22. Bierschenk, D. M.; Potter-Nelson, E.; Hoel, C.; Liao, Y.; Marks, L.; Poeppelmeier, K. R.; Barnett, S. A. Pd-Substituted (La,Sr)$CrO_{3-\delta}$–$Ce_{0.9}Gd_{0.1}O_{2-\delta}$ Solid Oxide Fuel Cell Anodes Exhibiting Regenerative Behavior. *J. Power Sources* **2011,** 196 (6), 3089-3094.

23. Madsen, B. D.; Kobsiriphat, W.; Wang, Y.; Marks, L. D.; Barnett, S. SOFC Anode Performance Enhancement through Precipitation of Nanoscale Catalysts. *ECS Trans.* **2007,** 7 (1), 1339-1348.

24. Neagu, D.; Tsekouras, G.; Miller, D. N.; Menard, H.; Irvine, J. T. *In situ* Growth of Nanoparticles through Control of Non-Stoichiometry. *Nat. Chem.* **2013,** 5 (11), 916-923.

25. Du, Z.; Zhao, H.; Yi, S.; Xia, Q.; Gong, Y.; Zhang, Y.; Cheng, X.; Li, Y.; Gu, L.; Swierczek, K. High-Performance Anode Material $Sr_2FeMo_{0.65}Ni_{0.35}O_{6-\delta}$ with *in Situ* Exsolved Nanoparticle Catalyst. *ACS Nano* **2016,** 10 (9), 8660-8669.

26. Myung, J. H.; Neagu, D.; Miller, D. N.; Irvine, J. T. Switching on Electrocatalytic Activity in Solid Oxide Cells. *Nature* **2016,** 537 (7621), 528-531.

27. Yang, C.; Li, J.; Lin, Y.; Liu, J.; Chen, F.; Liu, M. *In situ* Fabrication of CoFe Alloy Nanoparticles Structured $(Pr_{0.4}Sr_{0.6})_3(Fe_{0.85}Nb_{0.15})_2O_7$ Ceramic Anode for Direct Hydrocarbon Solid Oxide Fuel Cells. *Nano Energy* **2015,** 11, 704-710.

28. Yang, C.; Yang, Z.; Jin, C.; Xiao, G.; Chen, F.; Han, M. Sulfur-Tolerant Redox-Reversible Anode Material for Direct Hydrocarbon Solid Oxide Fuel Cells. *Adv. Mater.* **2012,** 24 (11), 1439-1443.

29. Chen, X.; Ni, W.; Wang, J.; Zhong, Q.; Han, M.; Zhu, T. Exploration of Co-Fe Alloy Precipitation and Electrochemical Behavior Hysteresis Using Lanthanum and Cobalt Co-Substituted $SrFeO_{3-\delta}$ SOFC Anode. *Electrochim. Acta* **2018,** 277 (1), 226-234.

30. Lai, K.-Y.; Manthiram, A. Evolution of Exsolved Nanoparticles on a Perovskite Oxide Surface during a Redox Process. *Chem. Mater.* **2018,** 30 (8), 2838-2847.

31. Lai, K.-Y.; Manthiram, A. Self-Regenerating Co-Fe Nanoparticles on Perovskite Oxides as a Hydrocarbon Fuel Oxidation Catalyst in Solid Oxide Fuel Cells. *Chem. Mater.* **2018,** 30 (8), 2515-2525.

32. Caignaert, V.; Millange, F.; Domenges, B.; Raveau, B.; Suard, E. A New Ordered Oxygen-Deficient Manganite Perovskite: $LaBaMn_2O_{5.5}$ Crystal and Magnetic Structure. *Chem. Mater.* **1999,** 11 (4), 930-938.

33. Kawasaki, Y.; Minami, T.; Izumi, M.; Kishimoto, Y.; Ohno, T.; Satoh, K. H.; Koda, A.; Kadono, R.; Gavilano, J. L.; Luetkens, H.; Nakajima, T.; Ueda, Y. μSR Investigation of Magnetically Ordered States in the A-site Ordered Perovskite Manganites $RBaMn_2O_6$ (R=Y and La). *Phys. Rev. B* **2012,** 86 (12), 125141.

34. Sengodan, S.; Choi, S.; Jun, A.; Shin, T. H.; Ju, Y. W.; Jeong, H. Y.; Shin, J.; Irvine, J. T.; Kim, G. Layered Oxygen-Deficient Double Perovskite as an Efficient and Stable Anode for Direct Hydrocarbon Solid Oxide Fuel Cells. *Nat. Mater.* **2015,** 14 (2), 205-209.

35. Sengodan, S.; Ju, Y.-W.; Kwon, O.; Jun, A.; Jeong, H. Y.; Ishihara, T.; Shin, J.; Kim, G. Self-Decorated MnO Nanoparticles on Double Perovskite Solid Oxide Fuel Cell Anode by in Situ Exsolution. *ACS Sustain. Chem. Eng.* **2017,** 5 (10), 9207-9213.

36. Kwon, O.; Sengodan, S.; Kim, K.; Kim, G.; Jeong, H. Y.; Shin, J.; Ju, Y. W.; Han, J. W.; Kim, G. Exsolution Trends and Co-Segregation Aspects of Self-Grown Catalyst Nanoparticles in Perovskites. *Nat. Commun.* **2017,** 8, 15967.

37. Choi, S.; Sengodan, S.; Park, S.; Ju, Y. W.; Kim, J.; Hyodo, J.; Jeong, H. Y.; Ishihara, T.; Shin, J.; Kim, G. A Robust Symmetrical Electrode with Layered Perovskite Structure for Direct Hydrocarbon Solid Oxide Fuel Cells: $PrBa_{0.8}Ca_{0.2}Mn_2O_{5+\delta}$. *J. Mater. Chem. A* **2016,** 4 (5), 1747-1753.

38. Sun, Y.-F.; Zhang, Y.-Q.; Hua, B.; Behnamian, Y.; Li, J.; Cui, S.-H.; Li, J.-H.; Luo, J.-L. Molybdenum Doped $Pr_{0.5}Ba_{0.5}MnO_{3-\delta}$ (Mo-PBMO) Double Perovskite as a Potential Solid Oxide Fuel Cell Anode Material. *J. Power Sources* **2016,** 301, 237-241.

39. Sun, Y. F.; Zhang, Y. Q.; Chen, J.; Li, J. H.; Zhu, Y. T.; Zeng, Y. M.; Amirkhiz, B. S.; Li, J.; Hua, B.; Luo, J. L. New Opportunity for in Situ Exsolution of Metallic Nanoparticles on Perovskite Parent. *Nano Lett.* **2016,** 16 (8), 5303-5309.

40. Zhao, L.; Chen, K.; Liu, Y.; He, B. A Novel Layered Perovskite as Symmetric Electrode for Direct Hydrocarbon Solid Oxide Fuel Cells. *J. Power Sources* **2017,** 342, 313-319.

41. Jun, A.; Kim, J.; Shin, J.; Kim, G. Achieving High Efficiency and Eliminating Degradation in Solid Oxide Electrochemical Cells Using High Oxygen-Capacity Perovskite. *Angew. Chem. Int. Ed.* **2016,** 55 (40), 12512-12515.

42. Hua, B.; Yan, N.; Li, M.; Sun, Y. F.; Zhang, Y. Q.; Li, J.; Etsell, T.; Sarkar, P.; Luo, J. L. Anode-Engineered Protonic Ceramic Fuel Cell with Excellent Performance and Fuel Compatibility. *Adv. Mater.* **2016,** 28 (40), 8922-8926.

43. Hou, N.; Li, P.; Lv, T.; Yao, T.; Yao, X.; Gan, T.; Fan, L.; Mao, P.; Zhao, Y.; Li, Y. $Sm_{0.5}Ba_{0.5}MnO_{3-\delta}$ Anode for Solid Oxide Fuel Cells with Hydrogen and Methanol as Fuels. *Catal. Today* **2017,** 298, 33-39.

44. Taskin, A. A.; Lavrov, A. N.; Ando, Y. Fast Oxygen Diffusion in A-site Ordered Perovskites. *Prog. Solid State Chem.* **2007,** 35 (2-4), 481-490.

45. Tomkiewicz, A. C.; Tamimi, M. A.; Huq, A.; McIntosh, S. Structural Analysis of $PrBaMn_2O_{5+\delta}$ under SOFC Anode Conditions by *in-Situ* Neutron Powder Diffraction. *J. Power Sources* **2016,** 330, 240-245.

46. Sun, Y.-F.; Li, J.-H.; Zhang, Y.-Q.; Hua, B.; Luo, J.-L. Bifunctional Catalyst of Core-Shell Nanoparticles Socketed on Oxygen-Deficient Layered Perovskite for Soot Combustion: *In Situ* Observation of Synergistic Dual Active Sites. *ACS Catal.* **2016,** 6 (4), 2710-2714.

47. Saracco, G.; Geobaldo, F.; Baldi, G. Methane Combustion on Mg-doped $LaMnO_3$ Perovskite Catalysts. *Appl. Catal. B-Environ.* **1999,** 20 (4), 277-288.

48. Cerri, I.; Saracco, G.; Specchia, V.; Trimis, D. Improved-Performance Knitted Fibre Mats as Supports for Pre-Mixed Natural Gas Catalytic Combustion. *Chem. Eng. J.* **2001,** 82 (1), 73-85.

49. Wang, Y.; Arandiyan, H.; Tahini, H. A.; Scott, J.; Tan, X.; Dai, H.; Gale, J. D.; Rohl, A. L.; Smith, S. C.; Amal, R. The Controlled Disassembly of Mesostructured Perovskites as an Avenue to Fabricating High Performance Nanohybrid Catalysts. *Nat. Commun.* **2017,** 8, 15553.

50. Liu, Y.; Zheng, H.; Liu, J.; Zhang, T. Preparation of High Surface Area $La_{1-x}A_xMnO_3$ (A= Ba, Sr or Ca) Ultra-Fine Particles Used for CH_4 Oxidation. *Chem. Eng. J.* **2002,** 89 (1), 213-221.

51. Liang, S.; Xu, T.; Teng, F.; Zong, R.; Zhu, Y. The High Activity and Stability of $La_{0.5}Ba_{0.5}MnO_3$ Nanocubes in the Oxidation of CO and CH_4. *Appl. Catal. B-Environ.* **2010,** 96 (3-4), 267-275.

52. Shao, Z.; Haile, S. M. A High-Performance Cathode for the Next Generation of Solid-Oxide Fuel Cells. *Nature* **2004,** 431 (47), 170-173.

53. Millange, F.; Caignaert, V.; Domenges, B.; Raveau, B.; Suard, E. Order-Disorder Phenomena in New $LaBaMn_2O_{6-\delta}$ CMR Perovskites. Crystal and Magnetic Structure. *Chem. Mater.* **1998,** 10 (7), 1974-1983.

54. Nakajima, T.; Kageyama, H.; Yoshizawa, H.; Ohoyama, K.; Ueda, Y. Ground State Properties of the A-site Ordered Manganites, $RBaMn_2O_6$ (R= La, Pr and Nd). *J. Phys. Soc. Jpn.* **2003,** 72 (12), 3237-3242.

55. Motohashi, T.; Ueda, T.; Masubuchi, Y.; Takiguchi, M.; Setoyama, T.; Oshima, K.; Kikkawa, S. Remarkable Oxygen Intake/Release Capability of $BaYMn_2O_{5+\delta}$: Applications to Oxygen Storage Technologies. *Chem. Mater.* **2010,** 22 (10), 3192-3196.

56. Spooren, J.; Walton, R. I.; Millange, F. A Study of the Manganites $La_{0.5}M_{0.5}MnO_3$ (M = Ca, Sr, Ba) Prepared by Hydrothermal Synthesis. *J. Mater. Chem.* **2005,** 15 (15), 1542-1551.

57. Zhu, T.; Troiani, H. E.; Mogni, L. V.; Han, M.; Barnett, S. A. Ni-Substituted $Sr(Ti,Fe)O_3$ SOFC Anodes: Achieving High Performance via Metal Alloy Nanoparticle Exsolution. *Joule* **2018**, 2 (3), 478-496.

58. Boukamp, B. A. Fuel cells: The Amazing Perovskite Anode. *Nat. Mater.* **2003,** 2 (5), 294-296.

59. He, W.; Wu, X.; Dong, F.; Ni, M. A Novel Layered Perovskite Electrode for Symmetrical Solid Oxide Fuel Cells: $PrBa(Fe_{0.8}Sc_{0.2})_2O_{5+\delta}$. *J. Power Sources* **2017,** 363, 16-19.

60. Sun, Y. F.; Li, J. H.; Cui, L.; Hua, B.; Cui, S. H.; Li, J.; Luo, J. L. A-site-deficiency Facilitated in situ Growth of Bimetallic Ni-Fe Nano-alloys: A Novel Coking-tolerant Fuel Cell Anode Catalyst. *Nanoscale* **2015,** 7 (25), 11173-11181.

61. Liu, S.; Liu, Q.; Luo, J.-L. CO_2-to-CO Conversion on Layered Perovskite with *in Situ* Exsolved Co-Fe Alloy Nanoparticles: an Active and Stable Cathode for Solid Oxide Electrolysis Cells. *J. Mater. Chem. A* **2016,** 4 (44), 17521-17528.

62. Kwon, O.; Kim, K.; Joo, S.; Jeong, H. Y.; Shin, J.; Han, J. W.; Sengodan, S.; Kim, G. Self-Assembled Alloy Nanoparticles in a Layered Double Perovskite as a Fuel Oxidation Catalyst for Solid Oxide Fuel Cells. *J. Mater. Chem. A* **2018,** 6 (33), 15947-15953.

63. Castner, D. G.; Watson, P. R.; Chan, I. Y. X-ray Absorption Spectroscopy, X-ray Photoelectron Spectroscopy, and Analytical Electron Microscopy Studies of Cobalt Catalysts. 2. Hydrogen Reduction Properties. *J. Phys. Chem.* **1990,** 94 (2), 819-828.

64. Ernst, B.; Bensaddik, A.; Hilaire, L.; Chaumette, P.; Kiennemann, A. Study on a Cobalt Silica Catalyst during Reduction and Fischer-Tropsch Reaction: *In Situ* EXAFS Compared to XPS and XRD. *Catal. Today* **1998,** 39 (4), 329-341.

65. Jacobs, G.; Ji, Y.; Davis, B. H.; Cronauer, D.; Kropf, A. J.; Marshall, C. L. Fischer-Tropsch Synthesis: Temperature Programmed EXAFS/XANES Investigation of the Influence of Support Type, Cobalt Loading, and Noble Metal Promoter Addition to the Reduction Behavior of Cobalt Oxide Particles. *Applied Catalysis A: General* **2007,** 333 (2), 177-191.

66. Zhu, J.; Liu, G.; Liu, Z.; Chu, Z.; Jin, W.; Xu, N., Unprecedented Perovskite Oxyfluoride Membranes with High-Efficiency Oxygen Ion Transport Paths for Low-Temperature Oxygen Permeation. *Adv. Mater.* **2016,** 28 (18), 3511-3515.

67. Zhi, M.; Zhou, G.; Hong, Z.; Wang, J.; Gemmen, R.; Gerdes, K.; Manivannan, A.; Ma, D.; Wu, N. Single Crystalline $La_{0.5}Sr_{0.5}MnO_3$ Microcubes as Cathode of Solid Oxide Fuel Cell. *Energy Environ. Sci.* **2011,** 4 (1), 139-144.

68. Du, Z.; Zhao, H.; Li, S.; Zhang, Y.; Chang, X.; Xia, Q.; Chen, N.; Gu, L.; Świerczek, K.; Li, Y.; Yang, T.; An, K. Exceptionally High Performance Anode Material Based on Lattice Structure Decorated Double Perovskite $Sr_2FeMo_{2/3}Mg_{1/3}O_{6-\delta}$ for Solid Oxide Fuel Cells. *Adv. Energy Mater.* **2018,** 8, 1800062.

69. Petitjean, M.; Caboche, G.; Siebert, E.; Dessemond, L.; Dufour, L.-C. $(La_{0.8}Sr_{0.2})(Mn_{1-y}Fe_y)O_{3\pm\delta}$ Oxides for ITSOFC Cathode Materials?: Electrical and Ionic Transport Properties. *J. Eur. Ceram. Soc.* **2005,** 25 (12), 2651-2654.

70. Wei, T.; Zhang, Q.; Huang, Y.-H.; Goodenough, J. B. Cobalt-Based Double-Perovskite Symmetrical Electrodes with Low Thermal Expansion for Solid Oxide Fuel Cells. *J. Mater. Chem.* **2012,** 22 (1), 225-231.

71. Wang, Z.; Tian, Y.; Li, Y. Direct CH_4 Fuel Cell Using Sr_2FeMoO_6 as an Anode Material. *J. Power Sources* **2011,** 196 (15), 6104-6109.

72. Zhang, L.; Yang, C.; Frenkel, A. I.; Wang, S.; Xiao, G.; Brinkman, K.; Chen, F. Co-Generation of Electricity and Chemicals from Propane Fuel in Solid Oxide Fuel Cells with Anode Containing Nano-Bimetallic Catalyst. *J. Power Sources* **2014,** 262, 421-428.

73. Liu, F.; Zhang, L.; Huang, G.; Niu, B.; Li, X.; Wang, L.; Zhao, J.; Jin, Y. High Performance Ferrite-Based Anode $La_{0.5}Sr_{0.5}Fe_{0.9}Mo_{0.1}O_{3-\delta}$ for Intermediate-Temperature Solid Oxide Fuel Cell. *Electrochim. Acta* **2017,** 255, 118-126.

74. Chung, Y. S.; Kim, T.; Shin, T. H.; Yoon, H.; Park, S.; Sammes, N. M.; Kim, W. B.; Chung, J. S. In Situ Preparation of a $La_{1.2}Sr_{0.8}Mn_{0.4}Fe_{0.6}O_4$ Ruddlesden-Popper Phase with Exsolved Fe Nanoparticles as an Anode for SOFCs. *J. Mater. Chem. A* **2017,** 5 (14), 6437-6446.

75. Shin, T. H.; Ida, S.; Ishihara, T. Doped CeO_2-$LaFeO_3$ Composite Oxide as an Active Anode for Direct Hydrocarbon-Type Solid Oxide Fuel Cells. *J. Am. Chem. Soc.* **2011,** 133 (48), 19399-19407.

76. Hua, B.; Li, M.; Sun, Y.-F.; Li, J.-H.; Luo, J.-L. Enhancing Perovskite Electrocatalysis of Solid Oxide Cells through Controlled Growth of Nanoparticles. *ChemSusChem* **2017,** 10 (17), 3333-3341.

77. Teng, F.; Chen, M.; Li, G.; Teng, Y.; Xu, T.; Hang, Y.; Yao, W.; Santhanagopalan, S.; Meng, D. D.; Zhu, Y. High Combustion Activity of CH_4 and Catalluminescence Properties of CO Oxidation over Porous Co_3O_4 Nanorods. *Appl. Catal. B-Environ.* **2011,** 110, 133-140.

78. Wang, H.; Chen, C.; Zhang, Y.; Peng, L.; Ma, S.; Yang, T.; Guo, H.; Zhang, Z.; Su, D. S.; Zhang, J., In Situ Oxidation of Carbon-Encapsulated Cobalt Nanocapsules Creates Highly Active Cobalt Oxide Catalysts for Hydrocarbon Combustion. *Nat. Commun.* **2015,** 6, 7181.

79. Hu, L.; Peng, Q.; Li, Y. Selective Synthesis of Co_3O_4 Nanocrystal with Different Shape and Crystal Plane Effect on Catalytic Property for Methane Combustion. *J. Am. Chem. Soc.* **2008,** 130 (48), 16136-16137.

80. Irvine, J. T. S.; Neagu, D.; Verbraeken, M. C.; Chatzichristodoulou, C.; Graves, C.; Mogensen, M. B. Evolution of the Electrochemical Interface in High-Temperature Fuel Cells and Electrolysers. *Nat. Energy* **2016,** 1 (1), 15014.

81. Neagu, D.; Oh, T. S.; Miller, D. N.; Menard, H.; Bukhari, S. M.; Gamble, S. R.; Gorte, R. J.; Vohs, J. M.; Irvine, J. T. Nano-Socketed Nickel Particles with Enhanced Coking Resistance Grown *in Situ* by Redox Exsolution. *Nat. Commun.* **2015,** 6, 8120.

82. Neagu, D.; Papaioannou, E. I.; Ramli, W. K. W.; Miller, D. N.; Murdoch, B. J.; Menard, H.; Umar, A.; Barlow, A. J.; Cumpson, P. J.; Irvine, J. T. S.; Metcalfe, I. S. Demonstration of Chemistry at a Point through Restructuring and Catalytic Activation at Anchored Nanoparticles. *Nat. Commun.* **2017,** 8 (1), 1855.

83. Huang, Y.-H.; Dass, R. I.; Denyszyn, J. C.; Goodenough, J. B. Synthesis and Characterization of $Sr_2MgMoO_{6-\delta}$. *J. Electrochem. Soc.* **2006,** 153 (7), A1266-A1272.

84. Huang, Y. H.; Liang, G.; Croft, M.; Lehtimäki, M.; Karppinen, M.; Goodenough, J. B. Double-Perovskite Anode Materials Sr_2MMoO_6 (M = Co, Ni) for Solid Oxide Fuel Cells. *Chem. Mater.* **2009,** 21 (11), 2319-2326.

85. Ding, H.; Tao, Z.; Liu, S.; Yang, Y. A Redox-Stable Direct-Methane Solid Oxide Fuel Cell (SOFC) with $Sr_2FeNb_{0.2}Mo_{0.8}O_{6-\delta}$ Double Perovskite as Anode Material. *J. Power Sources* **2016,** 327, 573-579.

86. Ding, H.; Tao, Z.; Liu, S.; Zhang, J. A High-Performing Sulfur-Tolerant and Redox-Stable Layered Perovskite Anode for Direct Hydrocarbon Solid Oxide Fuel Cells. *Sci. Rep.* **2015,** 5, 18129.